Research Article Vol. 31, No. 11 / 22 May 2023 / Optics Express 17836
Optics EXPRESS

Development of periodically concentric rings within microcavity upon femtosecond laser irradiation

RUIYAN LI,[1,2] TINGTING ZOU,[1,2] XIUYUN LI,[3,4,5] ZHI YU,[6,7] AND JIANJUN YANG[1,2,*]

[1] *GPL Photonics Laboratory, State Key Laboratory of Luminescence and Applications, Changchun Institute of Optics, Fine Mechanics and Physics, Chinese Academy of Sciences, Changchun, Jilin, 130033, China*
[2] *University of Chinese Academy of Sciences, Beijing 100049, China*
[3] *Single-Cell Center, CAS Key Laboratory of Biofuels, Shandong Key Laboratory of Energy Genetics, Qingdao Institute of Bioenergy and Bioprocess Technology, Chinese Academy of Sciences, Qingdao, China*
[4] *Shandong Energy Institute, Qingdao, China*
[5] *Qingdao New Energy Shandong Laboratory, Qingdao, China*
[6] *Shenyang National Laboratory for Materials Science, Institute of Metal Research, Chinese Academy of Sciences, Shenyang 110016, China*
[7] *zyu@imr.ac.cn*
[*] *jjyang@ciomp.ac.cn*

Abstract: Understanding the formation mechanisms of the nanostructures and their designs has important implications for both the fundamental science and application prospects. In this study, we proposed a strategy for femtosecond laser-induced high regularity concentric rings within silicon microcavity. The morphology of the concentric rings can be flexibly modulated by the pre-fabricated structures and the laser parameters. The physics involved is deeply explored by the Finite-Difference-Time-Domain simulations, which reveals that the formation mechanism can be attributed to the near-field interference of the incident laser and the scattering light from the pre-fabricated structures. Our results provide a new method for creating the designable periodic surface structures.

1. Introduction

The formation of large-area concentric rings has attracted extensive research interest in many application fields, such as surface-enhanced Raman scattering [1,2], surface-enhanced fluorescence [3,4], plasmonic lens fabrication [5,6], laser beam shaping [5,7], and high-sensitivity photodetection [8]. The current existing high-precision fabrication techniques such as the focused ion beam milling [2,6], the electron-beam lithography [7,9] and the lack-of-flexibility template [10,11], are more or less limited by their requirements for the cost and complex procedures. Nowadays, femtosecond (fs) laser has been proven useful for the nanoscale fabrication by taking advantage of its unique capabilities in the reduced thermal effect, flexible 3D design and suitability for a wide range of materials [12–15]. Several research groups have reported on using femtosecond laser in the manufacture of concentric ring structures with periods ranging from several micrometres to dozens of micrometres [16–20].

In recent years, the periodic surface structures induced by femtosecond laser have been a subject of intensive study, because of their self-organized features in the subwavelength and even nanometer scales to demonstrate wide potential applications in the visible light range [21,22]. Usually, the basic mechanism of laser-induced periodic structure (LIPSS) is attributed to the optical interference between the incident light and its excited surface plasmon polaritons (SPP). The already achieved variable geometric morphologies of LIPSSs such as one-dimensional (1D) grating-like structures [22–25], two-dimensional (2D) dot-matrix structures [26,27] and 2D

#486531 https://doi.org/10.1364/OE.486531
Journal © 2023 Received 30 Jan 2023; revised 3 Apr 2023; accepted 17 Apr 2023; published 11 May 2023

triangular structures [28], can be mainly related to the change of the incident laser polarization and the mode of the surface wave excitation. Hence a key to the formation of concentric rings is to generate the circularly periodic energy distribution by modulating the excited surface wave. Because of the difficulty in the surface wave regulation, there are a few reports about the laser-induced concentric rings only through using either the vector beam [29,30] or the single-spot irradiation with orthogonally polarized fs laser double-pulse sequences [31], but all of which have a low preparation efficiency and the irregular structure morphology. To settle this problem, several researchers have proposed some methods to manipulate the excited surface waves by the scattering of boundaries [32,33], the excitation mode of SPP [23,34,35], and the near field enhancement [36,37], which will help to finally induce the concentric ring structures.

In this paper, we introduce the pre-fabricated cylindrical cavities with different diameters as the scattering source to modulate surface wave excitation. The cylindrical focusing of circularly polarized fs laser can induce the concentric rings with a large area and high precision. Surprisingly, the concentric rings can be flexibly manipulated in the morphology with varying laser parameters and the pre-fabricated cavities. The simulation results revealed that the underlying mechanism is attributed to the near-field interference of the incident and the scattered lights. Of course, at the high laser energy density, the excitation of SPP can help to form the traditional grating-like LIPSS on the surface. Moreover, our further experiment demonstrated the concentric ring structures can be utilized for the fluorescence enhancement.

2. Experimental

Preparation of microcavity structures: In order to efficiently achieve the near-field wave excitation for the incident light, the cylindrically-shaped structures arrays with the unit dimension in micrometer scales were pre-fabricated on the surface of a crystalline silicon wafer (100) via the inductively coupled plasma etcher method.

Femtosecond laser-induced morphologicaly change: A schematic diagram of our experimental setup for the fs laser microprocessing is schematically illustrated in Fig. 1 where the employed laser source is a commercially available chirped pulse amplification of Ti sapphire fs laser system (Spectra-Physics HP-Spitfire 50) system, associated with the central wavelength of 800 nm, the repetition rate of 1 kHz and the time duration of 40 fs. The incident laser energy was controlled by a combination of a Glan prism and a half-wave plate. A quarter-wave plate (zero-order air gap achromatic quartz plate) was used for changing the fs laser pulse from the linear polarization into the elliptical or circular one. When the frequency-doubled fs laser is required, a beta-barium-borate (BBO) crystal with a spectral band-pass filter can be inserted after the Glan prism. The laser beam was focused by a cylindrical lens (focal length $f = 50$ mm) into a narrow line-shaped spot with a spatial width of 31 μm and length of 8 mm, respectively. The pre-fabricated microcavity sample was fixed on a 3D translating stage for precise movements. The surface morphology of the sample was characterized by both a scanning electron microscope (SEM, HITACHI, S-4800) and a laser confocal microscope (Keyence, VK-X1000). The material modification in the laser irradiation area were measured by Micro-Raman spectroscopy (Horiba Jobin Yvon) employing a 532 nm laser.

Photoluminescence of quantum dots: In this work, the $CsPbBr_3$ quantum dots were synthesized by hot injection and rapid cooling methods [38]. Then the 0.625 mg/mL quantum dots were dispersed in a 50 μL n-hexane solution and finally spin-coated on the sample surface at the rotation speed of 1500 r/min. The photoluminescence of the quantum dots film was measured by a HORIBA Scientific Raman spectrometer with a 473 nm laser incidence in air at room temperature.

Theoretical simulations: During the fs laser interaction with the material, the spatial distribution of the electric (E) field was simulated with the FDTD method (Lumerical software package). Both the top and bottom boundaries are totally set as perfectly matched layers (PML), and other

Optics EXPRESS

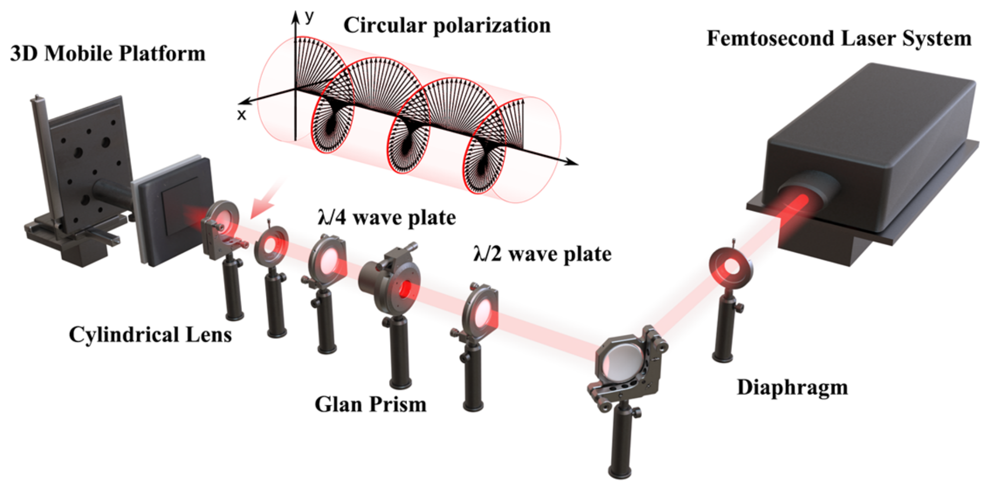

Fig. 1. A schematic of the femtosecond laser processing on the sample.

boundaries are provided with periodic boundary conditions. The employed parameters within the simulation model such as the light wavelength and polarization state, the feature dimensions and the optical index of the pre-fabricated structures, are properly given according to the experimental conditions.

3. Results and discussion

3.1. Concentric rings formed within the pre-fabricated structures

Figure 2(A) presents a diagram for the procedure of the concentric rings formation within the pre-fabricated structures, where the femtosecond laser beam is cylindrically focused for the large-area exposure with the scanning speed of $v = 0.6$ mm/s along the direction parallel to the sample surface. Figure 2(B) shows the SEM images of the pre-fabricated two-dimensional cylindrical cavity arrays before the laser irradiation, each of which possesses a diameter of ϕ=8 μm and an etching height of H = 800 nm, respectively. After the laser irradiation, it is surprising to see the concentric rings periodically formed inside the microcavities, as shown in Fig. 2(C), where the adopted laser fluence is $F = 28$ mJ/cm^2. From the corresponding high-definition SEM image (Fig. 2(D)), we can intuitively find that the numbers and the spatial period of the rings are N = 5 and Λ=845 nm, respectively. As shown in Fig. S1, the measured Raman spectrum of the non-irradiated surface region only presents a strong peak centered at 520.5 cm^{-1}, which characterizes the monocrystalline property. In contrast, the obtained Raman spectrum of the laser-induced ring surface possesses a broad band peak centered at 473 cm^{-1}, which represents the existence of amorphous silicon. Therefore, with our laser irradiation conditions, the resultant ring-like structures within the microcavity undergo the transformation from the monocrystalline to amorphous phases. The modulation depth of such nanoscale rings was measured at approximately d = 34 nm by using a laser confocal microscope (Fig. 2(E)). In sharp contrast to the conventional observation of both grating-like LIPSSs and other 2D structure arrays [26,34], here the laser-induced surface morphology is actually constituted by the regular distribution of concentric rings in the submicron scales, which indicates the physical roles of the cavity edges.

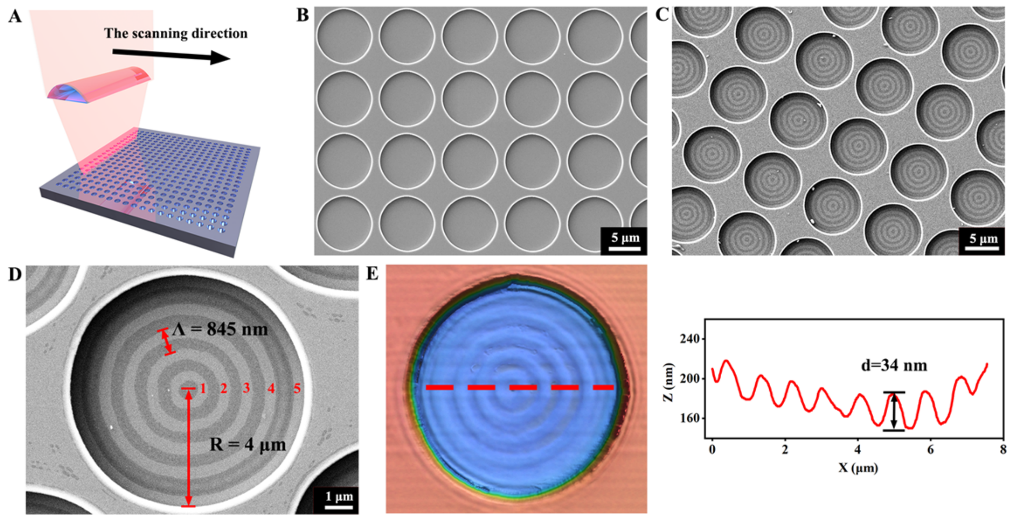

Fig. 2. Formation and geometric characterization of concentric rings. (A) Schematic diagram of the laser scanning procedures. (B) SEM image of the pre-fabricated microcavity arrays on the silicon surface. (C) SEM image of the surface structures after the laser scanning. Here the laser energy fluence is F = 28 mJ/cm^2 and the sample moving velocity is v = 0.6 mm/s. (D) High-resolution SEM image of (C). (E) A 3D picture of the concentric rings with the measured height information (the red dotted line).

3.2. Active modulation of concentric rings

The influence of cavity dimensions: In order to clarify how the formation of such periodically concentric rings is affected by the experimental parameters, we subsequently carried out a series of experiments to investigate this issue. First, we explored the dependence of the concentric rings on the pre-fabricated cylindrical cavity dimensions (in both diameter and depth). When the cavity diameter was varied from ϕ=4 μm to 10 μm under the fixed etching height of H = 800 nm, we can clearly see that the numbers of the concentric ring formation are ready to increase from N = 3 to 5, but still maintaining the spatial period around Λ=850 nm, as shown in Fig. 3(A). On the other hand, when the etching height of the cylindrical cavity changed from H = 400 nm to 1500 nm for the given diameters (ϕ=4 and 6 μm, respectively), the measured spatial period of the concentric rings was found to gradually increase, as shown in Fig. 3(B). Therefore, it can be concluded that the available numbers and the spatial period of the concentric rings are respectively determined by the diameter and the height of the pre-fabricated cylindrical cavity on Si surface.

The effect of laser wavelength: As is well known from the previous studies, the incident laser parameters play a significant role in affecting the geometric profiles of the traditional LIPSSs [39,40]. For example, the LIPSS period can be altered with different incident light wavelengths. To clarify this possible happening during our concentric ring formation, we used a BBO crystal to reduce the incident laser wavelength from λ=800 nm to 400 nm by frequency doubling, and then the generation of concentric rings can be still found within the cylindrical cavities, but associated with the smaller spatial period of around Λ=400 nm, as shown in Fig. 4. Very similar to the case of λ=800 nm laser incidence, the numbers of the concentric rings are demonstrated to gradually increase with larger cavity diameters (Figs. 4(A)–4(D)).

The dependence of laser polarization: Furthermore, the polarization state of the incident fs laser is also a key factor for modulating the morphology of LIPSS [41,42]. Figures 5(A)-(D) show the evolution of the induced concentric morphology with the laser polarization. In the case of linear polarization, the aforementioned concentric rings began to have a discontinuous distribution

Optics EXPRESS

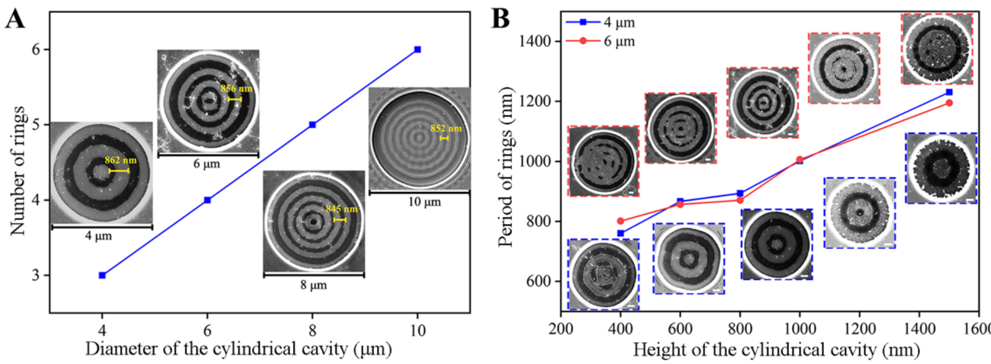

Fig. 3. Influence of cavity dimensions on the geometry of concentric rings. (A) The corresponding number of rings with different diameters of cavities. (B) The corresponding measured period of the rings with different heights of cavities. The inset SEM images represent the observations at different conditions.

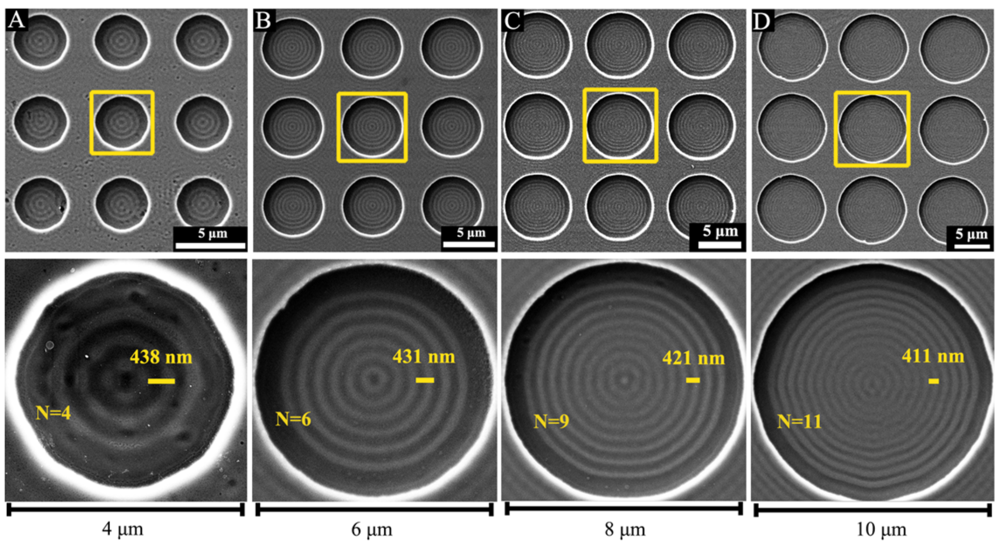

Fig. 4. Observed concentric ring structures in the pre-fabricated cavities with different diameters for the incident laser wavelength of 400 nm. The diameters of the structures in (A)-(D) are 4μm, 6μm, 8μm and 10μm, respectively. Here the laser energy fluence is $F = 8$ mJ/cm^2 and the sample moving velocity is $v = 0.4$ mm/s. The SEM images at the bottom line represent the enlarged situations in the yellow boxes above.

within the cavity, i.e., the formation of each concentric structure is spatially interrupted into two arch profiles. Remarkably, no laser-induced structures can take place along the radial directions that possess the small angles relevant to the laser polarization, as shown in Fig. 5(A). As the ellipticity (a ratio between the lengths of the minor and major axes) of the incident elliptically polarized light increases from ε=0.2 to 0.5, the spatial arrangement of the concentric ring-like structures become gradually continuous within the cylindrical cavities. As a matter of fact, with gradually increasing the energy fluence of the incident linearly polarized laser, the formation of the concentric rings began to re-appear and subsequently evolved into the periodic fringes with orientation perpendicular to the laser polarization direction, as shown in Fig. 6, the measured period of which is about 626 nm, less than that of the concentric rings. In other words, we can

Optics EXPRESS

understand that the observed periodic fringes at the high laser energy fluence conditions should belong to the traditional grating-like LIPSS phenomenon. All in all, for our experiment two types of the laser-induced periodic structures can be formed inside the cavities: one is the concentric rings with the period longer than the laser wavelength at the low incident energy fluence, and the other is the traditional grating-like LIPSS with the period smaller than the laser wavelength at the high incident energy fluence.

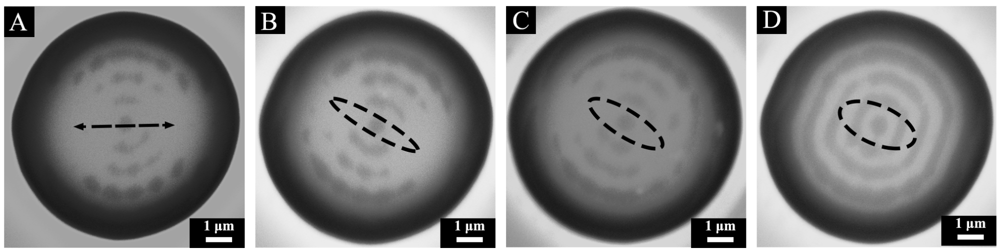

Fig. 5. The effect of laser polarization on the geometry of concentric rings. (A) Linear polarization, (B)-(D) Elliptical polarization with different ellipticities (ε=0.2, 0.33, and 0.5 respectively). Here the incident laser energy fluence is $F = 8$ mJ/cm^2 with the moving velocity of $v = 0.4$ mm/s. The cavity parameters are 8 µm in diameter and 800 nm in height. The black dotted lines represent the polarization situations.

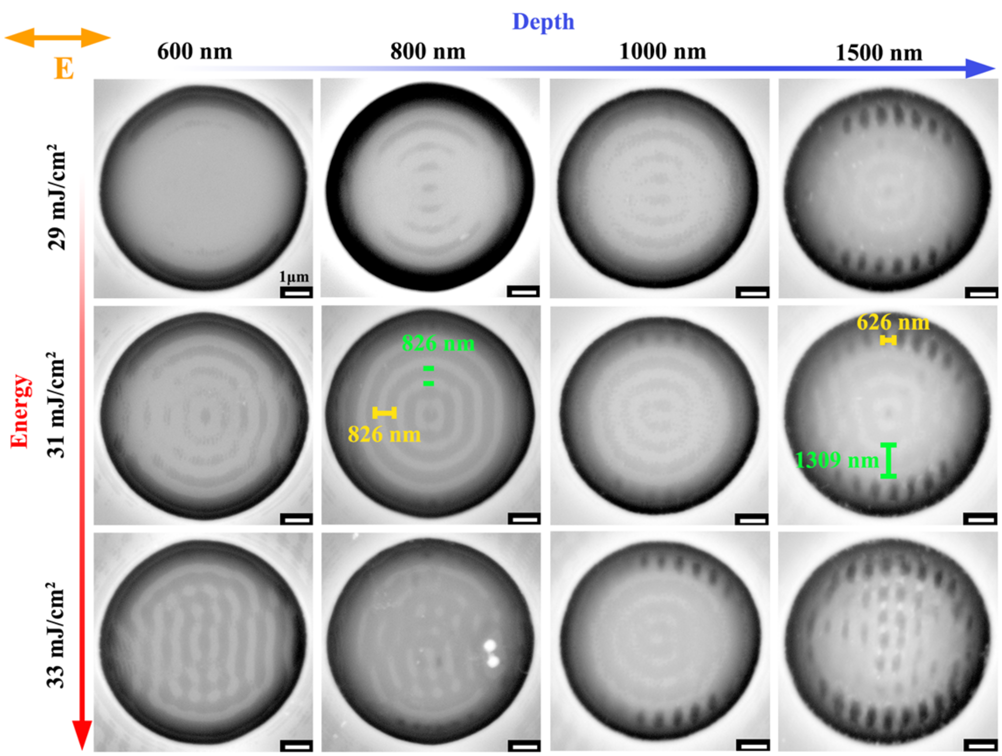

Fig. 6. Comparison of structures morphology through the different irradiation energies of the linearly polarized femtosecond laser with 800 nm wavelength. The prefabricated structures are all 8 microns in diameter during processing and from 600 to 1500 nm in depth. The scale bars are 1 µm.

Optics EXPRESS

3.3. Underlying mechanisms of the concentric rings formation

In order to comprehensively understand the formation mechanisms of the concentric rings within the cylindrical cavities, we applied the FDTD method to simulate the physical process, during which the diameter of the cylindrical cavity is set as ϕ=8 μm with varying the etching height from H = 600 nm to 1500 nm, and the laser polarization is assumed linearly in the horizontal direction. When the incident laser fluence is relatively low, the substrate silicon material is considered to have a refractive index of n = 3.688 + 0.006i at the wavelength of λ=800 nm, and the calculation results are shown in Figs. 7(A)-(D). It is clear that the concentrically periodic intensity distributions begin to appear at the bottom of the cylindrical cavity, especially with the pronounced patterns along the radial directions having the larger angles relevant to the laser polarization, which has a period larger than the laser wavelength as the type I shown in Fig. 7(I). In addition, with increasing the cavity height, the simulated numbers of the concentric ring formation are seen to decrease. On the other hand, when the laser energy fluence becomes relatively high, the silicon material can be optically excited, leading to a change in the permittivity value. For example, at the free carrier density of $N = 7.5 \times 10^{21}$ cm^{-3}, the calculated permittivity is ready to become ε^* = -15.3 + 2.4i [43], which makes the silicon material transfer into a metal-like state for the SPP excitation. Accordingly, the simulation results are shown in Figs. 7(E)-(H). Here, the permittivity change allows the SPP excitation to also form the periodic strip intensity distributions perpendicular to the polarization direction, which has a period smaller than the laser wavelength superimposed with the concentrically periodic intensity distributions (Type II) as shown in Fig. 7(I).

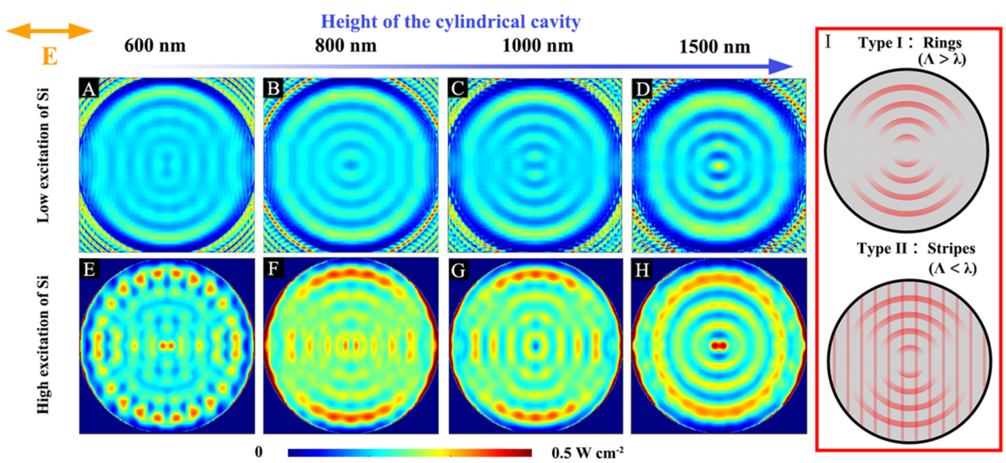

Fig. 7. Simulation results of E-field distribution on the different parameters of cylindrical cavities. The different height cylindrical cavities are of H = 600 nm, 800 nm, 1000 nm and 1500 nm under the low energy excitation (A)-(D) and the high energy excitation (E)-(H). (I) Schematic illustration of two different types of LIPSS.

After that, we carried out an in-depth numerical analysis of the modulation effect from the pre-fabricated cavity structure irradiated by the linearly polarized light, and the corresponding model is shown in Fig. 8(A), where the cavity diameter and height are given by 8 μm and 800 nm, respectively; and the refractive index of Si material has a tabulated value. In comparison with the simulation result in the x-z plane (Fig. 8(B)), the calculated E-field distribution demonstrates a clear periodic patterning in the y-z plane (Fig. 8(C)). In other words, the obtained intensity fringes of the E-field appear to be pronounced with the high visibility especially along the radial direction perpendicular to the light polarization. Here, the interference phenomenon between the incident laser and the boundary scattering light occurs in the near-field range of the propagation,

Optics EXPRESS

where the scattered lights in the x-z plane and y-z plane (Figs. 8(B and C) can be regarded as the cavity boundaries produce the reflected light under the P-wave and S-wave incidence respectively as shown in Fig. 9(A). Compared with P-wave incidence, the mode of S-wave incidence has the higher reflectivity and the phase does not change abruptly (Fig. 9(B)), so the scattered light under the S-wave incidence has the higher and clear periodic E-field distribution in the optical interference theory [44].

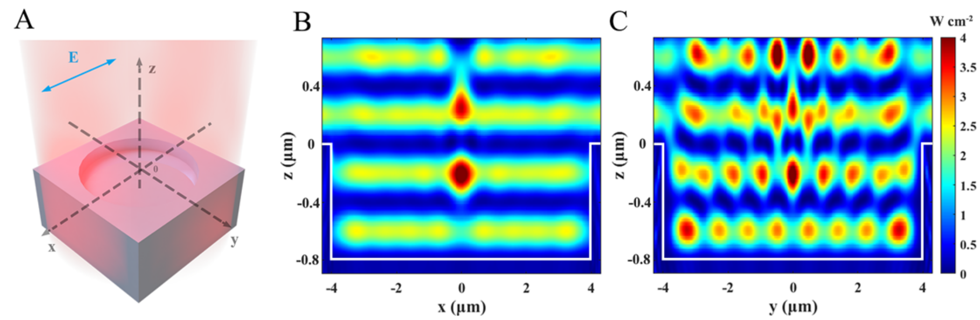

Fig. 8. (A) Schematic diagram of the incident 800 nm wavelength of the linearly polarized light along the z-axis from the top. Simulated spatial E-field distributions in the x-z plane (B) and y-z plane (C).

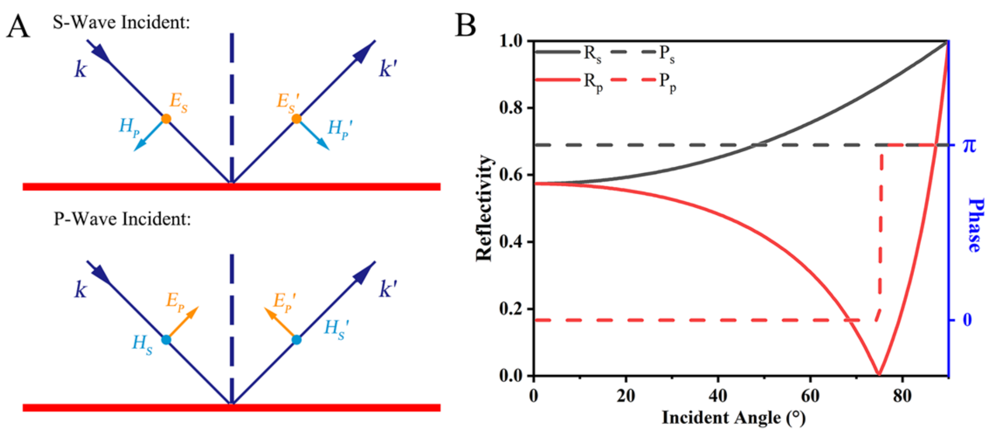

Fig. 9. Irradiating the silicon surface with different incident modes. (A) Schematic illustration of two irradiation types. (B) Reflectivity and phase change of silicon surface with two irradiation types.

In addition, according to the optical interference theory for two beams, the visibility of the intensity fringes is also determined by the interfering term of $I_{12} \propto cos\alpha$, where α is an intersection angle between directions of the linear polarization for two lights involved [44] [45]. In order to further explore the influence of the cavity boundary scattering on the laser polarization, we only consider the effect of the upper boundary of the cylindrical cavity on the interference, thus simplifying the model into a circular hole on the Si plate, as shown in figure 10A. For the available E-field distribution in the x-z plane, as shown in Fig. 10(B), the boundary scattering would like to result in almost no periodic patterns, in particular associated with varying the vector directions (the white arrows). However, for the obtained situation in the y-z plane, it can be found from Fig. 10(C) that the boundary scattering tends to make the E-field distribution exhibit not only the clear periodic patterns but also the unchangeable vector direction (the white arrows) with

Optics EXPRESS

respect to the incident light polarization. The physical reason for this phenomenon is essentially due to the phase-matching conditions of the electromagnetic wave propagation at the boundary, which requires that the variations of electric and magnetic components should be continuous in the tangential direction [44]. That is, the change of polarization direction for the scattering light depends on the spatial orientation of the cavity boundary relative to the incident light polarization. The polarization change becomes stronger for their perpendicular replacement. In fact, when the polarization property of the scattered light can be well maintained, the value of the interfering term $I_{12} \propto cos\alpha$ would like to reach the maximum, thus leading to the clear observation of the periodic fringes. In addition, from Fig.10C we can find that the spacing of interference fringes seems to increase with larger z values, which can be certainly used for explaining the observed positive correlations between the pre-fabricated structure height and the concentric ring period. The physical reason for this phenomenon is essentially due to the ring period $\Lambda \propto D$, where D is the distance from the source to the interference position [46].

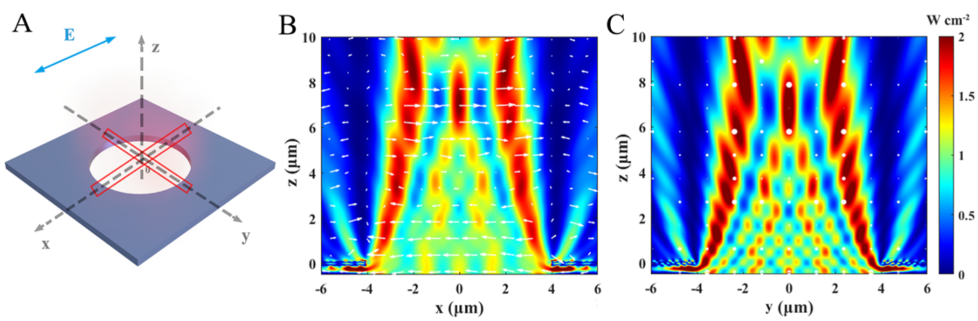

Fig. 10. (A) Schematic diagram of the incident 800 nm wavelength of linearly polarized light along the z-axis from the top. The blue arrow is the polarization direction, and the red lines represent the positions of the monitors. (B) and (C) are the simulated electric field distributions on the x-z and y-z planes, respectively, and the white arrows in the figure are the E field vectors.

Based on the above discussion, we can confirm that the observed spatial discontinuity of the concentric rings formation is attributed to the polarization change by the scattering of the cavity boundary, whose orientation is continuously varied relative to the incident linearly polarized laser. Thus, both the integrity and the continuity of the concentric rings can be controlled by changing the polarization state of the incident light, as shown in Fig. 11. Under the light incidence with the ellipticity of ε=0.2 (the intensity difference of the light polarization along the long and short axis directions is large), the formation of concentric rings is clearly seen to a have the non-uniform intensity distribution, the strong parts of which are mainly located on the specific arc areas with the large intersection angles between the radial directions and the long axis of the elliptically polarized light. As the ellipticity of the incident light increases (Figs. 11(B) to (D)), the intensity difference of the light polarization along the long and short axis directions becomes small, so that the strong intensity of concentric rings begins to be annularly extended, eventually leading to the spatial continuity for the incident circular polarization of the light. All of these simulations are well consistent with the experimental results. Now we can understand that the formation of concentric submicron rings within the cylindrical cavity physically originated from the near-field interference between the incident and the boundary scattering lights. Of course, this method is also applicable to manufacturing other types of structures (Fig. S2) by the incident circularly polarized laser onto the quadrangular and triangular cavity.

Optics EXPRESS

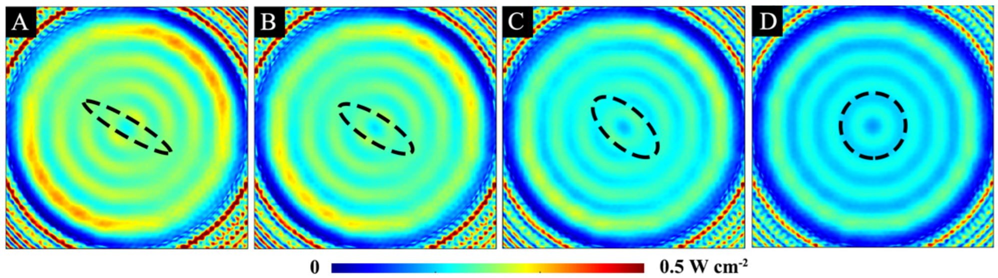

Fig. 11. Simulation E-field distribution results for the incident lights with different elliptical polarizations. (A)-(D) The ellipticities of the light are ε=0.2, 0.33, 0.5 and 1, respectively. Here, the cylindrical cavity has 8 μm in diameter and 800 nm in height, which is illuminated by the 800 nm wavelength of the light, and the black dotted line patterns in the figure are polarization states.

3.4. Application of the concentric rings for fluorescence enhancement

To confirm the potential capability of the aforementioned concentric ring structures, we carried out an additional experiment to test the fluorescence emission behaviors of the perovskite quantum dots on them, as shown in Fig. 12(A), where the laser excitation source has a wavelength of $\lambda_L = 473$ nm. It is clear that the measured peak intensity of the fluorescence on the concentric ring structures is about 8.5 times higher than that of the smooth surface. Through adopting the FDTD method with the incident circular polarization of the light, we also simulated the E-field distribution on the bottom of cylindrical cavity with and without concentric ring structures, as shown in Figs. 12(B) and (C). Evidently, in the case of the concentric rings the calculated E-field tends to exhibit a strong intensity at the central spot and it gradually decreases towards the outer rings, however, all of which are significantly higher than those of the smooth surface. Therefore, we can reasonably attribute the improved fluorescence measurement to the near-field enhanced excitation of the incident light, which indicates the light-converging function of the concentric rings within the cavity. Meanwhile, Fig. S3 shows the E-field enhancement effect at the center of the concentric rings for the incident light with different wavelengths, which is also helpful for improving the surface enhanced fluorescence in the future.

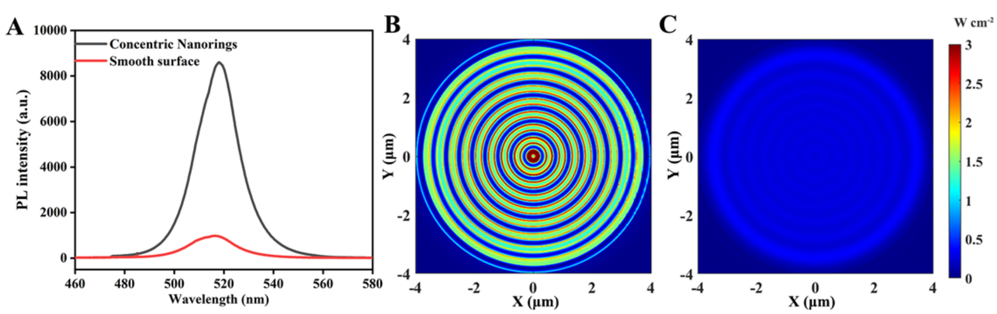

Fig. 12. (A) The measured photoluminescence intensity spectra of perovskite quantum dots for two different situations. Simulation results of E-field distribution on the bottom of cylindrical cavity with (B) and without (C) the concentric ring structures.

4. Conclusion

In summary, we introduce a new method to fabricate micro or nanostructures which are flexibly controlled on the geometric morphology. Through the FDTD simulations, we have deeply investigated the underlying mechanisms of concentric rings formation which is the near-field interference of the incident laser and the scattering light from the pre-fabricated structure. This method will help to produce some new types of micro/nano-structures by designing pre-fabricated structures to control the near-field interference in the future, which combines the laser scanning to achieve large-area and high-efficiency fabrication. In addition, we have preliminarily explored the enhanced fluorescence of concentric rings, which proves the ability of concentric rings to converge surface waves.

Funding. Strategic Priority Research Program of Chinese Academy of Sciences (XDA22010302); Jilin Provincial Science & Technology Development Project (20200201086JC); China Postdoctoral Science Foundation (2022M713068, 2022T150633).

Disclosures. The authors declare no conflicts of interest.

Data availability. Data underlying the results presented in this paper are not publicly available at this time but may be obtained from the authors upon reasonable request.

Supplemental document. See Supplement 1 for supporting content.

References

1. D. Wang, T. Yang, and K. B. Crozier, "Optical antennas integrated with concentric ring gratings: electric field enhancement and directional radiation," Opt. Express **19**(3), 2148–2157 (2011).
2. G. F. S. Andrade, Q. Min, R. Gordon, and A. G. Brolo, "Surface-Enhanced Resonance Raman Scattering on Gold Concentric Rings: Polarization Dependence and Intensity Fluctuations," J. Phys. Chem. C **116**(4), 2672–2676 (2012).
3. F. Prins, D. K. Kim, J. Cui, E. De Leo, L. L. Spiegel, K. M. McPeak, and D. J. Norris, "Direct Patterning of Colloidal Quantum-Dot Thin Films for Enhanced and Spectrally Selective Out-Coupling of Emission," Nano Lett. **17**(3), 1319–1325 (2017).
4. O. Mey, F. Wall, L. M. Schneider, D. Gunder, F. Walla, A. Soltani, H. Roskos, N. Yao, P. Qing, W. Fang, and A. Rahimi-Iman, "Enhancement of the Monolayer Tungsten Disulfide Exciton Photoluminescence with a Two-Dimensional Material/Air/Gallium Phosphide In-Plane Microcavity," ACS Nano **13**(5), 5259–5267 (2019).
5. J. X. Ji, Y. G. Meng, L. Sun, X. Y. Wu, and J. Wang, "Strong Focusing of Plasmonic Lens with Nanofinger and Multiple Concentric Rings Under Radially Polarized Illumination," Plasmonics **11**(1), 23–27 (2016).
6. W. Chen, D. C. Abeysinghe, R. L. Nelson, and Q. Zhan, "Plasmonic Lens Made of Multiple Concentric Metallic Rings under Radially Polarized Illumination," Nano Lett. **9**(12), 4320–4325 (2009).
7. Z. Ghadyani, I. Vartiainen, I. Harder, W. Iff, A. Berger, N. Lindlein, and M. Kuittinen, "Concentric ring metal grating for generating radially polarized light," Appl. Opt. **50**(16), 2451–2457 (2011).
8. J. Zeng, J. Gao, T. S. Luk, N. M. Litchinitser, and X. Yang, "Structuring Light by Concentric-Ring Patterned Magnetic Metamaterial Cavities," Nano Lett. **15**(8), 5363–5368 (2015).
9. N. A. Cinel, S. Cakmakyapan, G. Ertas, and E. Ozbay, "Concentric Ring Structures as Efficient SERS Substrates," IEEE J. Select. Topics Quantum Electron. **19**(3), 4601605 (2013).
10. Y. S. Jung, W. Jung, and C. A. Ross, "Nanofabricated concentric ring structures by templated self-assembly of a diblock copolymer," Nano Lett. **8**(9), 2975–2981 (2008).
11. S. W. Hong, J. Xu, and Z. Q. Lin, "Template-assisted formation of gradient concentric gold rings," Nano Lett. **6**(12), 2949–2954 (2006).
12. S. L. Diedenhofen, D. Kufer, T. Lasanta, and G. Konstantatos, "Integrated colloidal quantum dot photodetectors with color-tunable plasmonic nanofocusing lenses," Light: Sci. Appl. **4**(1), e234 (2015).
13. R. R. Gattass and E. Mazur, "Femtosecond laser micromachining in transparent materials," Nat. Photonics **2**(4), 219–225 (2008).
14. A. Y. Vorobyev and C. Guo, "Direct femtosecond laser surface nano/microstructuring and its applications," Laser Photonics Rev. **7**(3), 385–407 (2013).
15. R. Stoian and J.-P. Colombier, "Advances in ultrafast laser structuring of materials at the nanoscale," Nanophotonics **9**(16), 4665–4688 (2020).
16. C. Florian, S. V. Kirner, J. Krüger, and J. Bonse, "Surface functionalization by laser-induced periodic surface structures," J. Laser Appl. **32**(2), 022063 (2020).
17. B. Lan, M.-H. Hong, S.-X. Chen, K.-D. Ye, Z.-B. Wang, G.-X. Chen, and T.-C. Chong, "Laser-Ablation-Induced Concentric Ring Structures," Jpn. J. Appl. Phys. **42**(Part 1, No. 8), 5123–5126 (2003).
18. F. Ma, J. Yang, Xiaonong Zhu, C. Liang, and H. Wang, "Femtosecond laser-induced concentric ring microstructures on Zr-based metallic glass," Appl. Surf. Sci. **256**(11), 3653–3660 (2010).
19. P. Lorenz, M. Klöppel, F. Frost, M. Ehrhardt, K. Zimmer, and P. Li, "Laser-induced circular nanostructures in fused silica assisted by a self-assembling chromium layer," Appl. Surf. Sci. **280**, 933–939 (2013).
20. U. Klotzbach, K. Washio, C. B. Arnold, P. Lorenz, M. Klöppel, M. Ehrhardt, K. Zimmer, and P. Schwaller, "Nanosecond laser-induced nanostructuring of thin metal layers and dielectric surfaces," in *Laser-based Micro- and Nanoprocessing IX*, (2015).

Optics EXPRESS

21. X. Zhang, Y. Jiang, R. Qiu, J. Meng, J. Cao, C. Zhang, Y. Zhao, and T. Lü, "Concentric ring damage on the front surface of fused silica induced by a nanosecond laser," Opt. Mater. Express **9**, 152965 (2019).
22. T. Zou, B. Zhao, W. Xin, Y. Wang, B. Wang, X. Zheng, H. Xie, Z. Zhang, J. Yang, and C. L. Guo, "High-speed femtosecond laser plasmonic lithography and reduction of graphene oxide for anisotropic photoresponse," Light: Sci. Appl. **9**(1), 69 (2020).
23. H. Xie, B. Zhao, J. Cheng, S. K. Chamoli, T. Zou, W. Xin, and J. Yang, "Super-regular femtosecond laser nanolithography based on dual-interface plasmons coupling," Nanophotonics **10**(15), 3831–3842 (2021).
24. J. Geng, W. Yan, L. Shi, and M. Qiu, "Surface plasmons interference nanogratings: wafer-scale laser direct structuring in seconds," Light: Sci. Appl. **11**(1), 189 (2022).
25. J. Geng, X. Fang, L. Zhang, G. Yao, L. Xu, F. Liu, W. Tang, L. Shi, and M. Qiu, "Controllable generation of large-scale highly regular gratings on Si films," Light: Advanced Manufacturing **2**, 273–281 (2021).
26. X. Li, R. Li, Z. Yu, J. Xing, W. Kong, Y. Wang, and J. Yang, "Deepening of nanograting structures on Si by a two-step laser spatial-selective amorphization strategy combined with chemical etching," Appl. Surf. Sci. **589**, 152965 (2022).
27. L. Wang, Q. D. Chen, X. W. Cao, R. Buividas, X. Wang, S. Juodkazis, and H. B. Sun, "Plasmonic nano-printing: large-area nanoscale energy deposition for efficient surface texturing," Light: Sci. Appl. **6**(12), e17112 (2017).
28. S. Durbach and N. Hampp, "Generation of 2D-arrays of anisotropically shaped nanoparticles by nanosecond laser-induced periodic surface patterning," Appl. Surf. Sci. **556**, 149803 (2021).
29. X. Zheng, B. Zhao, J. Yang, Y. Lei, T. Zou, and C. Guo, "Noncollinear excitation of surface plasmons for triangular structure formation on Cr surfaces by femtosecond lasers," Appl. Surf. Sci. **507**, 144932 (2020).
30. E. Skoulas, A. Manousaki, C. Fotakis, and E. Stratakis, "Biomimetic surface structuring using cylindrical vector femtosecond laser beams," Sci. Rep. **7**(1), 45114 (2017).
31. W. Liu, J. Hu, L. Jiang, J. Huang, J. Lu, J. Yin, Z. Qiu, H. Liu, C. Li, S. Wang, and S. Wang, "Formation of laser-induced periodic surface nanometric concentric ring structures on silicon surfaces through single-spot irradiation with orthogonally polarized femtosecond laser double-pulse sequences," Nanophotonics **10**(4), 1273–1283 (2021).
32. G. Obara, N. Maeda, T. Miyanishi, M. Terakawa, N. N. Nedyalkov, and M. Obara, "Plasmonic and Mie scattering control of far-field interference for regular ripple formation on various material substrates," Opt. Express **19**(20), 19093–19103 (2011).
33. L. Chen, Z. Chen, K. Shimada, M. Mizutani, and T. Kuriyagawa, "Laser–induced nanopillar structures around particles," Appl. Surf. Sci. **572**, 151453 (2022).
34. R. Li, X. Li, T. Zou, W. Fu, J. Xing, T. Huang, Z. Yu, and J. Yang, "Deep investigation of two-dimensional structure arrays formed on Si surface," Appl. Surf. Sci. **605**, 154615 (2022).
35. P. N. Terekhin, J. Oltmanns, A. Blumenstein, D. S. Ivanov, F. Kleinwort, M. E. Garcia, B. Rethfeld, J. Ihlemann, and P. Simon, "Key role of surface plasmon polaritons in generation of periodic surface structures following single-pulse laser irradiation of a gold step edge," Nanophotonics **11**(2), 359–367 (2022).
36. Y. Tanaka, N. N. Nedyalkov, and M. Obara, "Enhanced near-field distribution inside substrates mediated with gold particle: optical vortex and bifurcation," Appl. Phys. A **97**(1), 91–98 (2009).
37. T. Sakai, Y. Tanaka, Y. Nishizawa, M. Terakawa, and M. Obara, "Size parameter effect of dielectric small particle mediated nano-hole patterning on silicon wafer by femtosecond laser," Appl. Phys. A **99**(1), 39–46 (2010).
38. L. Protesescu, S. Yakunin, M. I. Bodnarchuk, F. Krieg, R. Caputo, C. H. Hendon, R. X. Yang, A. Walsh, and M. V. Kovalenko, "Nanocrystals of Cesium Lead Halide Perovskites (CsPbX(3), X = Cl, Br, and I): Novel Optoelectronic Materials Showing Bright Emission with Wide Color Gamut," Nano Lett. **15**(6), 3692–3696 (2015).
39. E. V. Golosov, A. A. Ionin, Y. R. Kolobov, S. I. Kudryashov, A. E. Ligachev, Y. N. Novoselov, L. V. Seleznev, and D. V. Sinitsyn, "Ultrafast Changes in the Optical Properties of a Titanium Surface and Femtosecond Laser Writing of One-Dimensional Quasi-Periodic Nanogratings of Its Relief," J. Exp. Theor. Phys. **113**(1), 14–26 (2011).
40. S. Hou, Y. Huo, P. Xiong, Y. Zhang, S. Zhang, T. Jia, Z. Sun, J. Qiu, and Z. Xu, "Formation of long- and short-periodic nanoripples on stainless steel irradiated by femtosecond laser pulses," J. Phys. D: Appl. Phys. **44**(50), 505401 (2011).
41. M. Huang, F. L. Zhao, Y. Cheng, N. S. Xu, and Z. Z. Xu, "Origin of Laser-Induced Near-Subwavelength Ripples: Interference between Surface Plasmons and Incident Laser," ACS Nano **3**(12), 4062–4070 (2009).
42. O. Varlamova, F. Costache, M. Ratzke, and J. Reif, "Control parameters in pattern formation upon femtosecond laser ablation," Appl. Surf. Sci. **253**(19), 7932–7936 (2007).
43. K. Sokolowski-Tinten and D. von der Linde, "Generation of dense electron-hole plasmas in silicon," Phys. Rev. B **61**(4), 2643–2650 (2000).
44. M. Born and E. Wolf, *Principles of optics: electromagnetic theory of propagation, interference and diffraction of light* (Elsevier, 2013).
45. J. Tervo, T. Setala, and A. T. Friberg, "Degree of coherence for electromagnetic fields," Opt. Express **11**(10), 1137–1143 (2003).
46. S. Teng, F. Li, J. Wang, and W. Zhang, "Near-field interference of slit doublet," J. Opt. Soc. Am. A **30**(11), 2273–2279 (2013).